Review

Review on Mechanical Thermal Properties of Superalloys and Thermal Barrier Coating Used in Gas Turbines

Sunguk Wee [1,†], Jeonghyeon Do [2,†], Kyomin Kim [3,†], Changho Lee [4,†], Changsung Seok [1,*], Baig-Gyu Choi [2,*], Yoonsuk Choi [4] and Woochul Kim [3,*]

[1] Department of Mechanical Engineering, Sungkyunkwan University, Suwon 440-746, Korea; sinkill2@naver.com

[2] High Temperature Materials Research Center, Korea Institute of Materials Science, 797 Changwondaero, Changwon, Gyeognam 641-831, Korea; jhdo84@kims.re.kr

[3] School of Mechanical Engineering, Yonsei University, Seoul 03722, Korea; kyomkim@yonsei.ac.kr

[4] School of Materials Science & Engineering, Pusan National University, Busan 46241, Korea; dlckdgh522@gmail.com (C.L.); choiys@pusan.ac.kr (Y.C.)

[*] Correspondence: seok@skku.edu (C.S.); choibg@kims.re.kr (B.-G.C.); woochul@yonsei.ac.kr (W.K.)

[†] The following authors contributed equally to presented work.

check for updates

Abstract: This paper describes the manufacturing method and properties of a superalloy as a gas turbine blade material and a thermal barrier coating to protect it. The development process of superalloy and characteristics of each casting method were introduced. In particular, the single crystal superalloys were analyzed for creep and tensile properties with temperature according to chemical composition. In addition, the theories of creep life prediction models were summarized and comparative analysis was performed. Finally, the manufacturing processes of thermal barrier coatings were introduced, and the characteristics and effects of mechanical, thermal, and durability characteristics of each manufacturing process are described. We believe that this comprehensive review will help not only the gas turbine industry/community, but also material scientists, measurement physicists/engineers, and theorists interested in superalloys and high-temperature ceramics.

Keywords: superalloys; thermal barrier coating; mechanical and thermal properties of superalloys and thermal barrier coatings

1. Superalloy

1.1. Evolution of Superalloys

Gas turbines used in aircraft engines are fabricated using various materials such as aluminum alloys, titanium alloys, steels, composite materials, and nickel-based superalloys. For turbine parts exposed to extreme operating conditions such as high temperature and stress, materials and component manufacturing techniques must be selected to improve engine performance and lifetime. Initially, the gas turbine engines (W1) designed by Frank Whittles used various types of stainless steels, which were later replaced by nickel-based superalloys such as Nimonic or Inconel that exhibit better heat resistance [1,2]. Nickel-based superalloys used in the initial gas turbines included wrought alloys. However, with the development of precision casting technology in the 1950s, thin part of blades or internal cooling flow paths could be applied to increase the operation temperature of the turbine blade. In addition, as the constraints on processing such as forging and rolling were reduced, the composition of the superalloy became more diverse, and the stability of engine parts also improved.

Directional solidification by the Bridgman method marked the breakthrough in the casting of turbine blades. Initially, precision parts were cast as polycrystals with many grain boundaries. After solidification slowly proceeded in one direction in the melting furnace to remove grain boundaries perpendicular to the stress axis, directional solidified (DS) blades were produced as the usable temperature was increased. In addition, a single crystal (SC) casting technology has been introduced to produce single crystal blades by selectively growing only one grain to eliminate all grain boundaries, resulting in a higher maximum operating temperature compared to that of DS blades. Single crystal blade technology was first applied to the JT9D-7R4 engine from Pratt and Whitney in 1982.

As the turbine entry temperature (TET) of air engines improved, manufacturing technologies for engine parts were developed. Superalloys were developed from the viewpoint of material science such as the fraction and shape of the main phase, and when the new process was developed, the composition of the alloy was optimized for the process.

Table 1 shows the representative alloys and their chemical compositions for casting superalloys. Unlike polycrystalline alloys and directionally solidified alloys, single crystal superalloys do not contain grain boundary hardening elements such as C, B, and Zr. In addition, the content of Cr decreases in the order of polycrystalline alloys, directionally solidified alloys, single crystal alloys, the contents of refractory elements such as Mo, W, Ta, and Re increase in the same order. In the case of single crystals, alloys have been developed with increased temperature stability by adding expensive elements such as Re and Ru. Therefore, single crystal superalloys are categorized into generations according to the Re and Ru contents. Single crystal alloys containing no Re are classified as the first generation, alloys containing two–three percent Re are classified as the second generation, and alloys containing five–six percent Re are classified as the third generation. The fourth and fifth generations refer to Ru-added alloys.

Table 1. Composition of cast superalloys.

Class	Alloy	Compositions (wt.%)														
		Cr	Co	Mo	W	Al	Ti	Ta	Nb	Re	Ru	Hf	C	B	Zr	Ni
Conventional Cast (CC)	IN-713LC	12	-	4.5	-	5.9	0.6	-	2	-	-	-	0.05	0.01	0.1	Bal
	IN-738LC	16	8.5	1.75	2.6	3.4	3.4	1.75	0.9	-	-	-	0.11	0.01	0.04	Bal
	René 80	14	9	4	4	3	4.7	-	-	-	-	0.8	0.16	0.015	0.01	Bal
	Mar-M247	8	10	0.6	10	5.5	1	3	-	-	-	1.5	0.15	0.015	0.03	Bal
DS 1st	Mar-M200Hf	8	9	-	12	5	1.9	-	1	-	-	2	0.13	0.015	0.03	Bal
	CM247LC	8.1	9.2	0.5	9.5	5.6	0.7	3.2	-	-	-	1.4	0.07	0.015	0.007	Bal
DS 2nd	CM186LC	6	9.3	0.5	8.4	5.7	0.7	3.4	-	3.0	-	1.4	0.07	0.015	0.005	Bal
	PWA1426	6.5	10	1.7	6.5	6	-	4	-	3.0	-	1.5	0.1	0.015	0.1	Bal
SC 1st	CMSX-2	8	5	0.6	8	5.6	1	6	-	-	-	-	-	-	-	Bal
	PWA1480	10	5	-	4	5	1.5	12	-	-	-	-	-	-	-	Bal
	René N4	9	8	2	6	3.7	4.2	4	0.5	-	-	-	-	-	-	Bal
	AM1	7	8	2	5	5	1.8	8	1	-	-	-	-	-	-	Bal
	RR2000	10	15	3	-	5.5	4	-	-	-	-	-	-	-	-	Bal
SC 2nd	CMSX-4	6.5	9.6	0.6	6.4	5.6	1	6.5	-	3	-	0.1	-	-	-	Bal
	PWA1484	5	10	2	6	5.6	-	9	-	3	-	0.1	-	-	-	Bal
	René N5	7	8	2	5	6.2	-	7	-	3	-	0.2	-	-	-	Bal
SC 3rd	CMSX-10	2	3	0.4	5	5.7	0.2	8	-	6	-	0.03	-	-	-	Bal
SC 4th	TMS-138	2.9	5.9	2.9	5.9	5.9	-	5.6	-	4.9	2	0.1	-	-	-	Bal
SC 5th	TMS-162	2.9	5.8	3.9	5.8	5.8	-	5.6	-	4.9	6	0.09	-	-	-	Bal
SC Re-free	CMSX-7	6	10	0.6	9	5.7	0.8	9	-	-	-	0.2	-	-	-	Bal
SC Low Re	CMSX-8	5.4	10	0.6	8	5.7	0.7	8	-	1.5	-	0.1	-	-	-	Bal

Research has been conducted to improve the temperature stability of single crystal superalloys, leading to the development of sixth-generation single crystal superalloys. However, second-generation alloys such as CMSX-4, René N5, and PWA1484 containing three percent Re are the most commonly used. Re is a rare element that is obtained by mining and during the production of Cu or Cu/Mo. Ru is a precious metal that can be obtained during the production of platinum. Not only do these alloying elements considerably increase the price of single crystal superalloys but they also lead to the issue of limited economic and strategic supply. Therefore, recently, various studies have been conducted on alloys with superior characteristics with reduced Re content to lower the prices of such super alloys. As commercial alloys, CMSX-8 containing 1.5% Re and CMSX-7 containing no Re have been developed by Cannon Muskegon [3].

1.2. Types of Casting Superalloys and Their Properties

1.2.1. Conventional Cast Alloys

Most polycrystal superalloys contain large amounts of chromium elements considering the oxidizing and corrosive environment formed during combustion of fuels, and elements such as carbon, boron, zirconium, and hafnium, which enhance grain boundaries to increase creep resistance, are added. Cr, Co, and Mo are distributed in the face-centered cubic (FCC) matrix to enhance the solid solution, and Cr forms a Cr_2O_3 oxide film, which plays a role in excellent high-temperature corrosion resistance. Ti, Ta, Nb, and V strengthen the γ' phase by substituting Al in Ni_3Al. In recent years, as the purity of fuel has increased, corrosion-producing products have decreased. In addition, because of the development of thermal barrier coatings (TBCs) to protect superalloy materials, elements to improve the temperature stability of alloys are more important than those that enhance the oxidation and corrosion resistance of superalloys.

Mechanical properties of conventional cast superalloys are shown in Figure 1. Mar-M247 shows higher strength than other alloys especially at high temperatures. In addition, the creep property of the Mar-M247 alloy is better than that of the other aforementioned alloys.
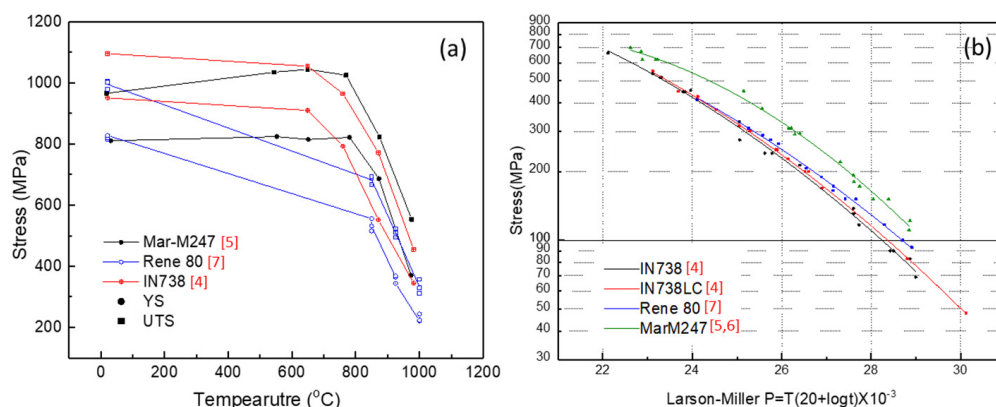

Figure 1. Mechanical properties of conventional cast superalloys, (**a**) strength, (**b**) Larson-Miller plot [4–7].

1.2.2. Directional Solidified Alloys

Polycrystal superalloys produced via the DS method considerably increase creep resistance by forming vertical grain boundaries to minimize the grain boundaries in the direction vulnerable to centrifugal force of the turbine blades.

Mar-M200Hf is an improved DS alloy from polycrystalline alloy Mar-M200, whose lateral ductility deterioration and grain boundary cracking is prevented during casting. Hf is added to Mar-M200 based on the report of Martin Metals, which showed that the stress rupture resistance at 760 °C and castability were improved when Hf was added to the alloy [8].

CM247LC was formulated by Cannon-Muskegon to adapt the Mar-M247 alloy to the DS process. To prevent grain boundary cracking during the casting process, the Zr and Ti contents were reduced and the minimum content of impurities such as Si and S was lowered. In addition, by controlling the C content, the ductility was improved in the temperature range from room temperature to the intermediate temperature range, and the amount of plate shape M_6C was reduced by controlling the W content [9].

CM186LC, a second-generation DS alloy, was developed by Cannon-Muskegon containing 3% Re to achieve high productivity and economic advantages and to secure heat resistance via the addition of Re [10]. In addition, this alloy is characterized by its excellent mechanical properties, which can be obtained without solution heat treatment. Therefore, there is less risk of recrystallization during solution treatment, and this alloy can be produced using revert of single crystal alloys such as CMSX-2, CMSX-3, and CMSX-4. Figure 2 shows the mechanical properties of the three alloys—Mar-M200Hf, CM247LC, and CM186LC. CM186LC shows better creep properties than the other alloys, especially at high temperature and low stress [10,11].
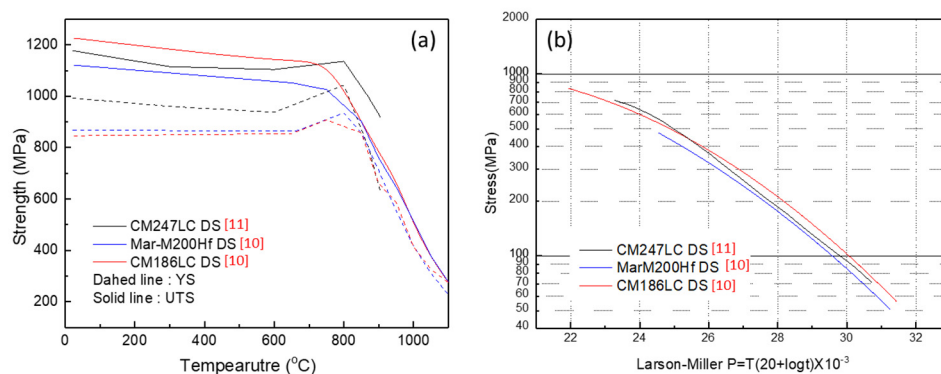

Figure 2. Mechanical properties of directional solidified (DS) superalloys, (**a**) strength, (**b**) Larson-Miller plot [10,11].

1.2.3. Single crystal superalloys

Similar to DS superalloys, single crystal superalloys were developed to increase the creep resistance and temperature acceptability by minimizing grain boundaries. Therefore, additive elements such as C, B, Zr, and Hf were removed from most single crystal superalloys to suppress the formation of grain boundaries. In addition, as heat treatment was possible at a higher temperature by removing the above added elements, it was possible to increase the fraction of the γ′ phase and improved microstructure uniformity.

- First-generation alloys

Single crystal alloys did not receive much attention initially because the creep, thermal fatigue, and oxidation resistance of conventionally heat-treated single crystal Mar-M200 are not significantly better than those of the DS alloy. Subsequently, it was found that the incipient melting temperature increased considerably when the grain boundary strengthening elements such as B, C, and Zr were removed. In addition, γ′ can precipitate finely and uniformly after complete dissolution without local melting when the incipient melting temperature increased, improving the creep properties of single crystals [12]. Based on these results, some single crystal superalloys have been developed.

René N4 was developed by GE. Cr and C contents in René N4 are increased to improve the hot corrosion resistance of René N, the first single crystal alloy developed by GE. The Al/Ti ratio was increased to enhance oxidation resistance, and Ta content was increased to compensate for the decrease in γ′ volume fraction due to Ti reduction. In addition, 0.15% Hf was added to improve the oxidation resistance, and B was added to prevent degradation of mechanical properties due to the creation of a low angle boundary [13].

PWA1480 developed by Pratt and Whitney was the first commercialized single crystal alloy among the PWA series in 1982 [14]. Increased Ta content improves the oxidation resistance and inhibits freckle formation, and sufficient Cr and Al are added for oxidation resistance. The alloying elements, Mo and V, were removed while maintaining a sufficiently high Cr content to obtain good hot corrosion resistance [15]. Yield strength and creep properties of some first-generation single crystal superalloys are shown in Figure 3.
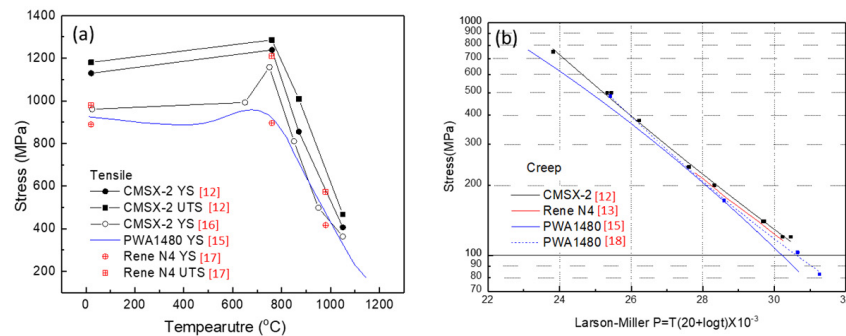
Figure 3. Mechanical properties of first-generation single crystal superalloys, (**a**) yield strength, (**b**) Larson-Miller plot [12–18].

- Second-generation alloys

CMSX-4 is a second-generation single crystal alloy developed by Canon-Muskegon in the early 1980s and has been used in gas turbines since it was first commercialized in 1991. The alloy was modified to CMSX-4 [SLS] with enhanced oxidation resistance in the 2000s.

René N5 is a second-generation single crystal alloy developed by GE. GE has also developed René N515 with 1.5% Re and a Re-free alloy, René N500, based on this alloy. René N5 is used not only for turbine blades but also in aircraft engines and power generation gas turbines.

PWA1484 was designed by Pratt and Whitney to exhibit approximately 50 °F (28 °C) higher temperature stability than PWA1480. In addition to the creep properties, various properties such as stability of the microstructure, castability, oxidation resistance, thermal fatigue resistance, and high cycle fatigue (HCF) properties were considered during development [14]. Then, 5.5% Al and 8.7% Ta were added to increase the solvus temperature of γ' and also to suppresses coarsening of γ' at high temperature and to maintain the volume fraction of γ' [14]. The mechanical properties of second-generation single crystal alloys, CMSX-4, René N5, and PWA1484, are compared and shown in Figure 4.
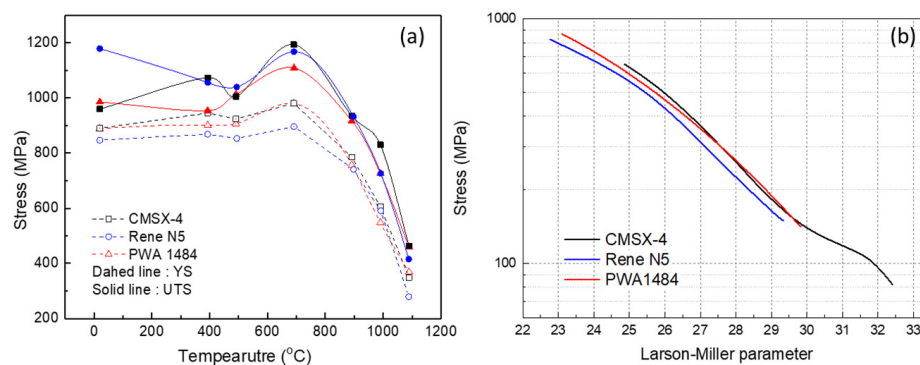
Figure 4. Mechanical properties of second-generation single crystal superalloys, (**a**) strength, (**b**) Larson-Miller plot [3,19].

- Third-generation single-crystal superalloys

Second-generation single crystal alloys have been successfully applied to gas turbines, but there is a demand for higher temperature stability. Representative third-generation single-crystal alloys include CMSX-10 [20] developed by Cannon Muskegon, GE's René N6 [21], and TMS75 and TMS80 alloys [22] developed by NIMS.

By increasing the Re content to 6%, CMSX-10, a third-generation single crystal alloy with a low Cr content for thermal stability, was developed by both increasing the content of other refractory elements and significantly changing the Al and Ti contents [20]. Creep strength of the alloy was improved by approximately 30 °C compared to the second-generation alloy. CMSX-10 has been modified to CMSX-10N with 7% of Re in which the compositions of other elements were slightly adjusted.

- Fourth- and fifth-generation single crystal superalloys

In the case of third-generation single crystal superalloys containing 5–6% of Re, the creep properties are found to be degraded because of the formation of topologically closed-packed (TCP) phases after a long duration under high temperatures. Several studies have found that the addition of ruthenium reduces the formation tendency of TCP [23–25]. Ru is preferentially distributed to γ, while Rh, Pd, and Pt are preferentially distributed to γ′ and Ir is almost evenly distributed on γ/γ′ [25]. In addition, the high temperature creep characteristics of fourth-generation single crystal alloys are very good. One of them is TMS-138 developed by NIMS in Japan, which has excellent hot corrosion resistance [26]. Caron [27] studied the development of the fourth generation of single crystal alloys by varying the content of Re and Ru and presented an alloy called MC-NG (Mono Cristal-Nouvelle Generation). The results show that the creep properties of MC-NG are nearly equivalent to those of the representative third-generation single crystal alloys, CMSX-10 and René N6, and the phase stability of TCP is excellent.

Based on TMS-138, fifth-generation single crystal alloys such as TMS-162 and TMS-173 with higher Ru content were developed [26]. They increased the Mo content from 2.9 to 3.9 wt.% and improved the stability of the TCP phase formation by increasing the Ru content. In addition, TEM confirmed that the dislocation network formed at the γ/γ′ interface was much finer and more regular than before. The temperature stability of TMS-162 is approximately 20 °C higher than that of TMS-138 at 1083 °C.

However, the oxidation resistances of TMS-162 and TMS-173 were degraded because of the low Cr content for microstructure stability. Therefore, the TMS-196 alloy was developed to improve creep, thermo-mechanical fatigue, phase stability, and oxidation resistance [28]. Figure 5 shows the creep rupture lives as Larson-Miller curves of three alloys, CMSX-10, TMS-138, and TMS-196 [20,28,29]. It can be seen that the creep properties are significantly improved in higher generation alloys, especially in the high-temperature low-stress regions.
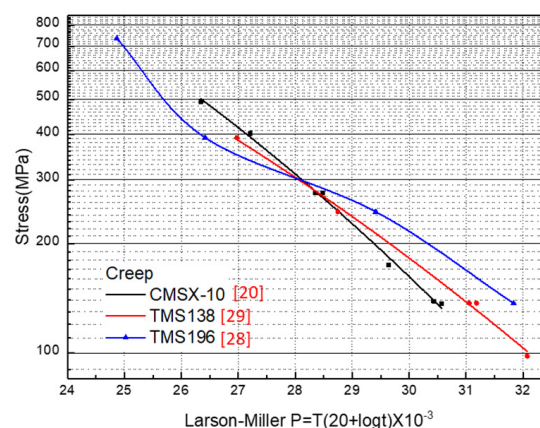

Figure 5. Larson-Miller plot of three different generations of single crystal superalloys [20,28,29].

- Cost effective superalloys

As mentioned above, Re and Ru are added into single crystal superalloys to increase the temperature stability, but these elements are expensive and their supply is strategically dangerous. Therefore, single crystal superalloys with less Re content that have superior properties to the first-generation single crystal alloys and comparable properties to the second-generation alloys have been developed in recent years. As commercial alloys, CMSX-8 containing 1.5% Re and CMSX-7 without Re were developed by Cannon-Muskegon [3]. In the case of CMSX-8, the composition was adjusted to CMSX-8[B/C] version with B and C addition to prevent degradation at high temperature due to low angle boundary (LAB).

A low-rhenium alloy, TMS-286, containing 1.2% Re for aircraft engine application with good corrosion resistance and mechanical properties was developed in Japan using their own alloy design program [30]. Re-free TMS-1700 for power generation gas turbines was also designed to exhibit better TMF properties than conventional first-generation superalloys. The creep properties of TMS-1700 are superior to those of CMSX-4 under low-temperature high-stress conditions (800 °C/735 MPa) and high-temperature low-stress conditions (1100 °C/137 MPa).

QTSX is the low Re (1%) single crystal superalloy designed by applying integrated computational material engineering technologies, which has comparable properties to second-generation single crystal superalloys [31].

Re-free low-density single crystal superalloy ERBO/15 was developed based on multi-criteria numerical optimization [32]. The alloy has a lower density than the second-generation single crystal superalloy, CMSX-4, and comparable creep properties, especially in the high-temperature low-stress regime.

1.3. Manufacturing Process for Casting Superalloys and High-Temperature Components

In the early stages of gas turbine blade manufacturing, many forging methods using nickel-based superalloys were used. However, as the γ′ volume fraction increased to improve high temperature strength, the high temperature formability decreased, and the manufacturing method was replaced by the casting method. Until recently, most turbine blades were manufactured using a casting method, which allows more precise and complex surface shaping.

Casting alloys are used to fabricate complex parts such as blades and vanes. They are generally cast under vacuum because they have some well-oxidized alloying elements such as Al and Ti. Based on the casting method, different microstructures of superalloys are formed. The microstructure shape is closely related to the thermal properties as well as the mechanical properties such as high temperature phase stability, tensile and yield strength, and creep resistance. Therefore, several casting methods have been developed to improve the mechanical and thermodynamic properties of superalloys.

Conventional cast superalloys have a polycrystalline grain structure. However, the grain boundary perpendicular to the major stress axis can degrade the creep properties at high temperatures. To improve the creep life of the casted alloys, directional solidification casting was developed to remove grain boundaries perpendicular to the stress axis, and a single crystal casting process was developed to remove all grain boundaries. Figure 6a shows blades with different grain shapes depending on the casting method.

A schematic diagram of Bridgman casting is shown in Figure 6b. Very fine grains are formed when the molten superalloy is poured into a mold preheated to approximately 1500 °C placed on a water-cooled Cu chills. A temperature gradient is generated in one direction between the upper part of the mold with the molten superalloy and the lower part which has already solidified. As a result, the crystal grows in one direction when the mold is gradually lowered. Nickel-based superalloys with FCC structure prefer to grow in the [001] direction during solidification. Dendrites aligned in the direction of the temperature gradient tend to grow rapidly in the [001] direction when the superheated liquid at the interface with the dendritic phase prevents the formation of new grains. Accordingly, columnar grains parallel to the solidification direction are formed after the casting process.
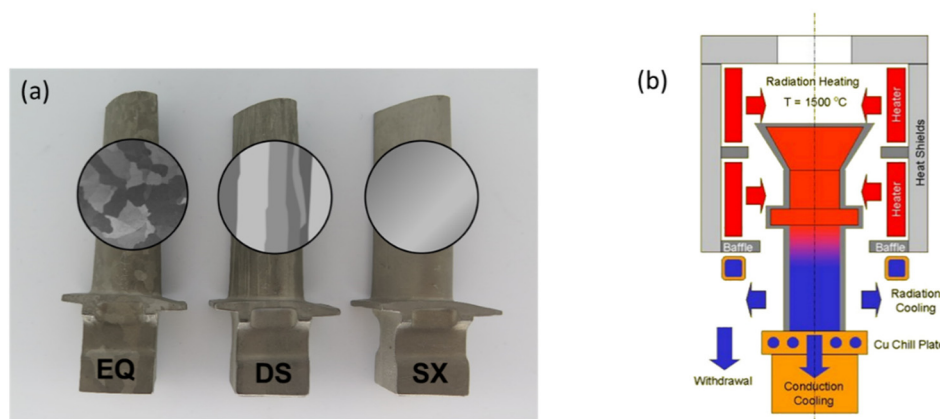
Figure 6. (**a**) Turbine blades with different grain structures according to the casting process, (**b**) schematic diagram of Bridgman casting system.

In the case of single crystal superalloy casting, as shown in Figure 7, solidification begins from the starter block in contact with the chill plate and proceeds to the selector. The number of grains decreases while passing through the starter block, as can be seen in Figure 7. The mechanism of competitive growth of grains in the starter block is the same as that of directional solidification. Among the many polycrystalline grains produced on chill plates, only some of the grains arranged in favor of the temperature gradient and growth survive to form a columnar structure as solidification progresses. A single grain is selected and grown through the selector among the several columnar grains entering the selector. Another way to cast single crystals is via the use of a seed. A single crystal seed is inserted underneath the mold when the mold is being fabricated. Unlike the selector method in which the single crystal grows in the [001] direction, this method has the advantage that the growth direction of the single crystal can be controlled because the crystal grows in the same direction as the seed.
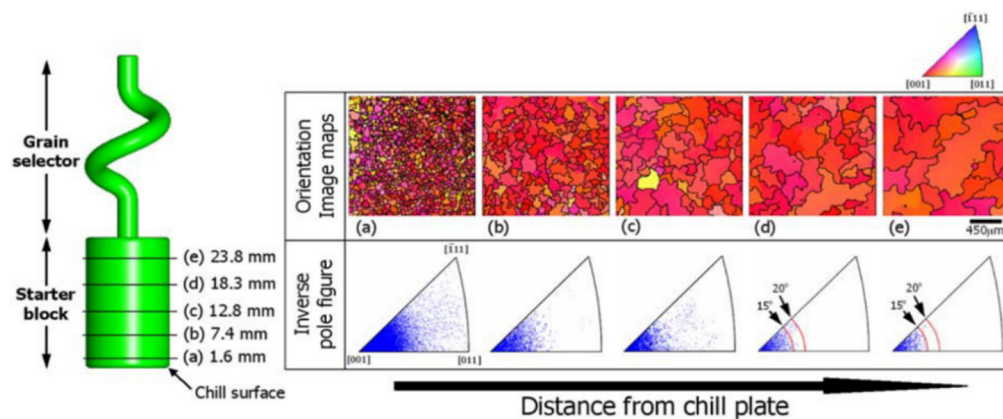

Figure 7. Electron backscatter diffraction (EBSD) orientation image map and corresponding inverse pole figures at various positions of the starter block (reproduced with permission from [33], Springer Nature, 2009).

In the conventional single crystal casting method, a temperature gradient is generated using a water-cooled Cu plate. However, a liquid metal cooling (LMC) method using a liquid metal like Sn as a coolant was introduced to increase the temperature gradient, because the larger the temperature gradient, the better the quality of casting. The LMC method is more effective than the conventional methods for casting larger components with a fine and homogeneous structure [34].

In the manufacturing of turbine components using superalloy machining processes, after casting such as grinding of the root form and drilling of the cooling hole is required. However, nickel-based alloys are considered as difficult-to-cut alloys due to several characteristics [35,36]. Nickel-based alloys

have an FCC structure, which shows a high degree of work hardening, leading to severe tool notch wear just in the depth of cut line on the cutting edge [36]. High hardness and high strength under elevated temperature with hard carbide and precipitates causes severe abrasion on tools and results in a deleterious effect on the tool wear rate [36]. Low thermal conductivity results in high temperatures at the tool tip [36]. Therefore, several studies [36–39] have been conducted to improve the machinability of superalloys and life of tools with ultrasonic vibration-assisted milling (UAM) [36,37] and machining with high pressure coolant (HPC) [38].

1.4. Thermal Properties of Superalloys

Because superalloys are exposed to high-temperature and high-pressure environments for a long time, many studies have been conducted on measuring the mechanical properties required to withstand these harsh environments. In addition, the thermal properties have also been studied. The higher the thermal conductivity of the superalloys, the easier the heat dissipation and cooling in the blade design. The uniform temperature distribution inside the blade has the advantage of reducing the thermal stress during operation by reducing the temperature gradient [40–42]. The thermal conductivity of superalloys is influenced by electrons because of the free electrons in the metal than by phonons due to lattice vibration. The chemical composition of superalloys influences the change in thermal conductivity, and the changes in thermal conductivity vary depending on how many types of materials that affect thermal conductivity are included based on nickel [41]. The inclusion of various chemical compositions enhances the mechanical properties of superalloys; however, these chemical compositions result in point defects in the nickel lattice, which reduce the thermal conductivity. Nickel, the base of nickel-based superalloys, has a thermal conductivity of approximately 106 W/m-K at room temperature, but as shown in Figure 8, alloys with various other metals have a thermal conductivity of 10–30 W/m-K, which is 10–30% that of nickel [43].
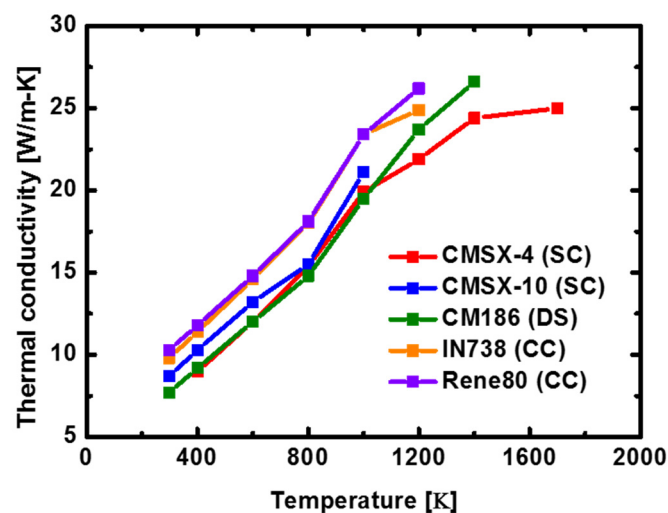

Figure 8. Variation of thermal conductivity of nickel-based superalloys with temperature according to casting method [44].

1.5. Creep Life Prediction Model

When high temperature and stress are applied to the material for a long time, the material undergoes permanent deformation, such as creep. At this time, the stress is less than the yield strength and the temperature is below the melting temperature. When creep deformation occurs, the material can mechanically degrade or break. Therefore, the study of creep is important to improve safety and reliability. However, it is difficult to experimentally obtain long-term creep data for more than 10,000 h, and the creep data are insufficient. Thus, the importance of research for predicting long-term creep life from relatively short-term creep experimental data is gradually increasing [45,46].

Commonly used creep life prediction models use approaches to predict long-term creep life by extrapolation using time-temperature parameters. This approach has the advantage of requiring a small amount of experimental data to derive the creep life prediction curve. As a model for predicting long-term creep life from short-term creep tests, the representative model is the Larson-Miller parameter (LMP) [46–48].

Recently, many predictive models have been studied based on the power law equation model, which represents the relationship between steady-state creep rate ε_{ss}, absolute temperature T, and stress σ in the form of the Arrhenius equation. The normalized power law model, Wilshire model were proposed by normalizing the stress term of the power law equation. In these cases, these models attempted to improve the stress term by adding a tensile stress term [45–49].

1.5.1. Traditional Power Law Creep Models

- Power model

The power law model represents the steady-state creep rate, ε_{ss}, as a function of temperature and stress. It can be expressed by combining the Arrhenius's law and Norton's law. Equations (1) and (2) represent Arrhenius's law and Norton's law, respectively [48,49]:

$$\dot{\varepsilon}_{ss} \propto \exp\left(\frac{-Q_c}{RT}\right) \tag{1}$$

$$\dot{\varepsilon}_{ss} \propto A\sigma^n \tag{2}$$

where ε_{ss} is the steady-state creep rate at temperature (T), Q_c is the creep activation energy, R is the ideal gas constant (8.314 J/mol-K), σ is the applied stress, A is a proportional constant, and n is the creep exponent. The Arrhenius Law indicates that the strain rate increases as the temperature (T) increases, and Norton's Law indicates that the strain rate increases as the stress (σ) increases.

The power law model can be expressed as Equation (3) by a combination of Equations (1) and (2).

$$\dot{\varepsilon}_{ss} \propto A\sigma^n \exp\left\{\frac{-Q_c}{RT}\right\} \tag{3}$$

where ε_{ss} is the steady-state creep rate at temperature (T), Q_c is the creep activation energy, R is the ideal gas constant, A is the proportional constant, and n is the creep exponent. In the case of power law, Q_c and n are assumed to be constant. The power law model represents the steady-state creep rate as a function of temperature and stress. In a creep deformation, when the temperature is increasing, dependence of stress on steady state creep rate is increasing. It is represented by a change in n value at the power law model [48,49]. It shows in Figure 9.
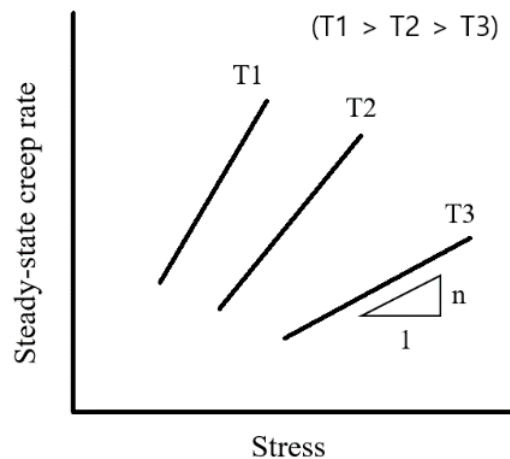

Figure 9. Schematic representation of steady-state strain rate versus stress.

- Larson-Miller parameter method

The most widely used creep life prediction method for metals is the LMP method. The LMP consists of two relationships: power law equation (Equation (3)) and Monkman-Grant relationship (Equation (4)).

$$\dot{\varepsilon}_{ss} t_r = C_{MG} \tag{4}$$

where ε_{ss} is the steady-state creep rate at temperature (T), C_{MG} are constants, and t_r is the rupture time in the creep test. Assuming constant stress, the two equations can be summarized as the following LMP equation (Equation (5)).

$$P_{LM} = f(\sigma) = T(C_{LM} + \log t_r) \tag{5}$$

where P_{LM} is the Larson-Miller parameter and C_{LM} is the Larson-Miller constant. C_{LM} typically has a value between 10 and 50. The LMP model predicts creep life based on empirical fitting. Using P_{LM}, LMP model can show a relationship between stress and P_{LM}. However, it has limitations in explaining the change of deformation mechanism when the stress and temperature is changing.

1.5.2. Modern Creep Model Approaches

Traditional creep models, which are based on the power law equation, are focused on extrapolating predictions using existing data trends. When using the traditional creep model, if the dominant creep deformation mechanism varies with temperature and stress, the creep life at low temperatures cannot be accurately predicted with results of creep tests performed at higher temperatures.

In recent years, many studies have been conducted to improve the predictability of creep life by solving the above problem. In particular, the method of normalizing stress to tensile strength is used often. Tensile strength is used rather than yield strength because it is the maximum strength that can be applied in the creep test and the value of tensile strength can be obtained more easily than that of yield strength. Normalized power law and Wilshire model are creep models normalizing with tensile strength [48,49].

- Normalized power law equation

The improvement of the stress term using the normalization factor from the power law model is called the normalized power law model. Such normalization factors include yield strength, tensile strength, and elastic modulus, but tensile strength is mainly used. This allows all creep data to be represented in the stress range from $\sigma/\sigma_{TS} = 0$ to $\sigma/\sigma_{TS} = 1$, and the temperature dependence of creep activation energy (Q_c) is improved.

Normalized power law gives as Equation (6)

$$\dot{\varepsilon}_{ss} \frac{M}{t_r} = A\left(\frac{\sigma}{\sigma_{TS}}\right)^n \exp\left(\frac{-Q_c^*}{RT}\right) \tag{6}$$

where ε_{ss} is the steady-state creep rate at temperature (T), Q_c^* is creep activation energy, A is constant, n is creep exponent, and M is Monkman-Grant constant. A and n value can be derived by linear relationship fitting of the x-axis with $\ln(\sigma/\sigma_{TS})$ and the y-axis with $\ln(\varepsilon_{ss} \exp(Q_c^*/RT))$. When representing the linear relationship of the NPL model, it is important to find the optimal Q_c^* value. If an optimal NPL linear relationship is made with experimental short-term creep data, it is possible to predict long-term creep life by extrapolation. When the deformation mechanism changes for each stress in the creep data, there may be multiple slopes in the NPL linear relationship [47]. With this model, it can be seen that the predictability is superior to the LMP model when predicting long-term creep life [45,47].

- Wilshire approach

The Wilshire model has been introduced to examine the long-term rupture strength by extrapolating the short-term creep measurements. The formula has been modified based on the normalized power law to make linear relationship between function of stress and rupture time.

$$\frac{\sigma}{\sigma_{TS}} = \exp\left\{-k_1\left[t_r\exp\left(\frac{-Q_c^*}{RT}\right)\right]^u\right\} \tag{7}$$

where σ is the creep stress, σ_{TS} is the tensile strength, t_r is the creep rupture time, Q_c^* is the creep activation energy, R is the ideal gas constant, and k_1 and u are constants. k_1 and u can be derived by linear relationship fitting the x-axis with $\ln(t_r\exp(-Q_c^*/RT))$ and the y-axis with $\ln(-\ln(\sigma/\sigma_{TS}))$ [50–53]. The Wilshire model is influenced by the Q_c^* value like the NPL model in the fitting of the linear relationship. Multiple slopes also exist according to change creep deformation mechanism [47]. However, in the case of the Wilshire model, it is possible to derive a creep life regardless of the Monkman-Grant relationship. In predictability regime, the Wilshire model shows better long-term creep life prediction accuracy compared to LMP, NPL model [47].

2. Thermal Barrier Coating

2.1. Background of Thermal Barrier Coating

Recently, various fields have been researched to improve the efficiency of mechanical systems operating in high-temperature harsh environments such as gas turbines. Improvements in efficiency in mechanical systems, in particular gas turbines, include prolonged operating life, high operating efficiency, and reduced emissions. To satisfy these conditions, increasing the thermodynamic efficiency by increasing the turbine entry temperature is the most effective, but as the operating temperature increases, a severe operating environment is created, which damages the core parts. Core components, such as TBCs, are applied to parts of gas turbines that are directly exposed to high-temperature environments. By applying low thermal conductivity coatings on components such as blades, the temperature of the components is reduced by approximately 100–300 °C. By using this technique, the gas turbine can be operated at a combustion gas temperature 250 °C higher than the melting temperature of the nickel-based superalloy. In addition, TBCs increase the service life of gas turbine components because they reduce the temperature of metal components [54,55]. These TBCs consist of a top coating of ceramic material that directly blocks the flames and reduces heat transfer and a metal material that binds the top coating and the base material, as shown in Figure 10. Top coatings are most commonly used with a ZrO_2 component called yttria stabilized zirconia (YSZ). In addition, YSZ has low thermal conductivity and high oxygen permeability [56]. Bond coating is a layer of metal material composed of MCrAlY (M: Co, Ni), which is used to prevent flame penetration into the superalloy base material and to relieve thermal stress due to the differences in thermal expansion coefficient between the superalloy and top coating. Because of the high oxygen permeability of the top coating, the Al component present in the bond coating reacts with the penetrated oxygen to form a thermally grown oxide (TGO). A TGO is formed on the bond coat layer with the α-Al_2O_3 component to protect the inner surface from further oxidation. To improve the adhesive strength before spraying the ceramic top coating layer, 2–3 μm of TGO are formed on the bond coating via proper heat treatment. However, the growth of 8–10 μm thick TGO during the operation of high-temperature components generates interfacial stress with the ceramic layer, reduces the adhesion, and causes TBC delamination [57]. Therefore, in the design of TBCs, consideration should be given to the TGO as well as the heat resistance, high temperature properties, and the techniques used for the deposition of coatings [56].
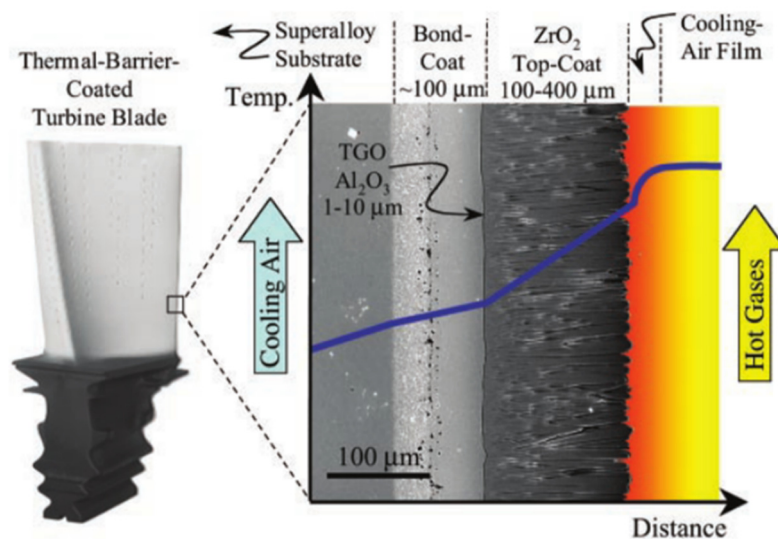
Figure 10. Scanning electron microscope (SEM) images of thermal barrier coating (TBC) (reproduced with permission from [58], The American Association for the Advancement of Science, 2002).

2.2. Type of TBC According to Manufacturing Process

The microstructure of TBCs depends on the material used as well as the manufacturing technique. The microstructure of the coating affects the required performances such as the thermal barrier performance and oxidation resistance, and also the coating durability; therefore, it is necessary to understand the coating manufacturing technique. TBCs have different deposition techniques depending on the temperature and material used. When choosing a TBC process, many aspects including performance, capital, process cost per part, thickness, composition, surface roughness requirements, and cooling hole cover should be considered. Such TBC methods include electron beam-physical vapor deposition (EB-PVD), chemical vapor deposition (CVD), and atmospheric plasma spray (APS) EB-PVD process is widely used even though it is an expensive process because it provides excellent thermal barrier performance, well-controlled composition and thickness. When coating with the PVD method, water droplets may be generated on the coating surface due to coating defects, which may negatively affect the surface processing [59]. EB-PVD proceeds as follows. First, the YSZ ingot is evaporated in a vacuum chamber by using an electron beam [60]. Prior to the deposition on the substrate, the substrate is preheated to 1000 °C under low oxygen partial pressure conditions to form a thin layer of TGO. Next, the surface of the substrate is coated by adjusting the environmental conditions in the vapor cloud. To ensure that the TBCs obtained through EB-PVD have high adhesion, the temperature of the base material during the process is 0.47 times that of the ceramic top coating material (YSZ). The microstructure of the TBC obtained through the EB-PVD process is shown in Figure 11. The EB-PVD process is particularly effective for matching the planar modulus of microstructures. For example, coating through the EB-PVD process makes columnar microstructures, resulting in a low planar modulus. This is an advantage in the generation of strain because of the mismatch in thermal expansion coefficients between the metal base material and the ceramic top coating [61,62].
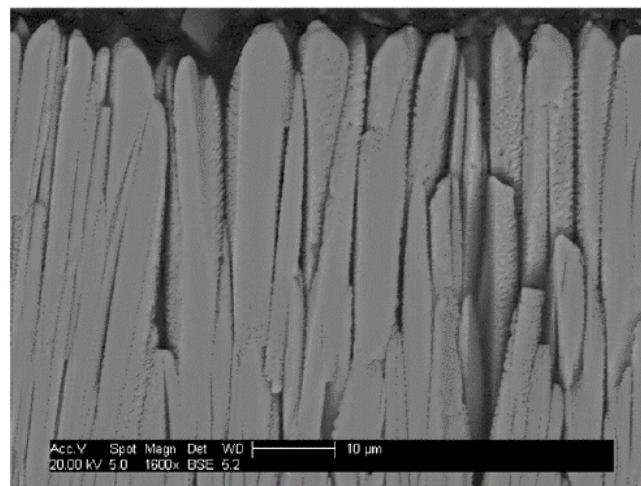
Figure 11. Cross-sectional view of as deposited electron beam-physical vapor deposition (EB-PVD) TBC microstructure (reproduced with permission from [63], Elsevier, 2015).

CVD is a fabrication technique with good coverage and uniform control of the microstructure [64]. It is often classified by the precursor material and energy source and uses a heat source such as an RF induction heater. Because CVD is usually used to coat thin films, deposition rates are usually slow; however, for non-oxides, optimization can be performed by optimizing the process parameters [65]. In contrast, for oxides, it is difficult to increase the deposition rate because of the uniform powder formation in the gas phase; this can be overcome by appropriately selecting the geometrical structural characteristics of the precursor and CVD chamber. Figure 12 shows a cross section of an YSZ coating deposited at 230 μm/h using laser CVD [66].
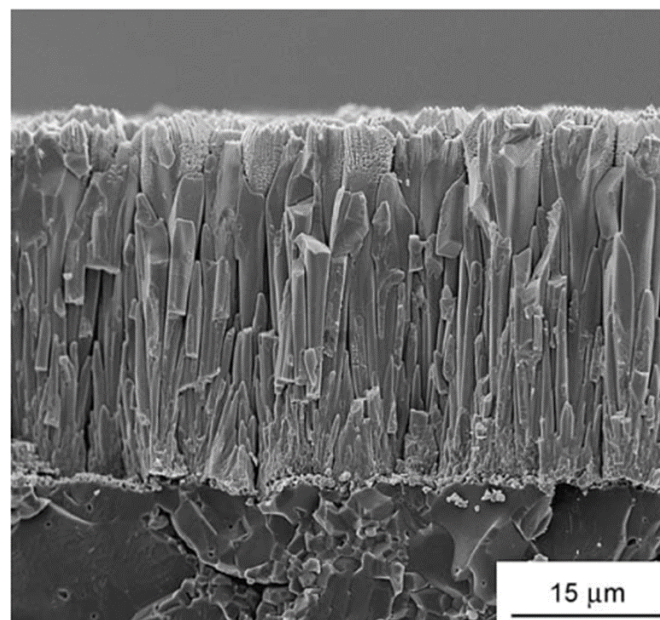

Figure 12. Microstructure of TBC manufactured by chemical vapor deposition (CVD) process (reproduced with permission from [66], Elsevier, 2005).

APS is a technique used to convert gases such as Ar, He, and N_2 into plasma and discharging them from a nozzle to achieve an ultra-high temperature and high-speed plasma jet as a heat source. Thermal spraying is essentially used for high melting point metals and ceramic coatings, and because of the high plasma jet speed, thermal spraying materials collide with the substrate at a high speed,

allowing the coating to exhibit high adhesion strength and high density. Its disadvantages are that the air is incorporated into the plasma jet flame, resulting in high porosity and weak adhesion, and oxides or nitrides are formed depending on the base material, which results in a coating with impurities. In general, the spray-type coating has granulated surfaces, so a finishing operation is necessary. Since the strength and toughness of the coating are limited, a detailed processing is required. This can be solved by using cutting inserts with sharp edges, and positive rake and flank angles [67]. During the APS process, α-Al_2O_3 (TGO) is formed from the bond coating during preheating, top coating deposition, and subsequent heat treatment. α-Al_2O_3 (TGO) formed with the optimum thickness and crystals is very important to prevent the regeneration and premature delamination of the TBCs. The optimal thickness of the TGO immediately after deposition is considered to be approximately 0.3–1.0 μm. APS shown in Figure 13 is mainly used for combustion chamber components, HPT shrouds, and power plant components because of their cost effectiveness and the ability to fit thick coatings. In particular, dense vertically cracked (DVC) microstructures are increasingly being used in various processes of APS. The coatings produced by this process have vertical cracks that provide resistance against strain, and have similar effectiveness as the cracks of EB-PVD, but at a much lower cost [54,68].
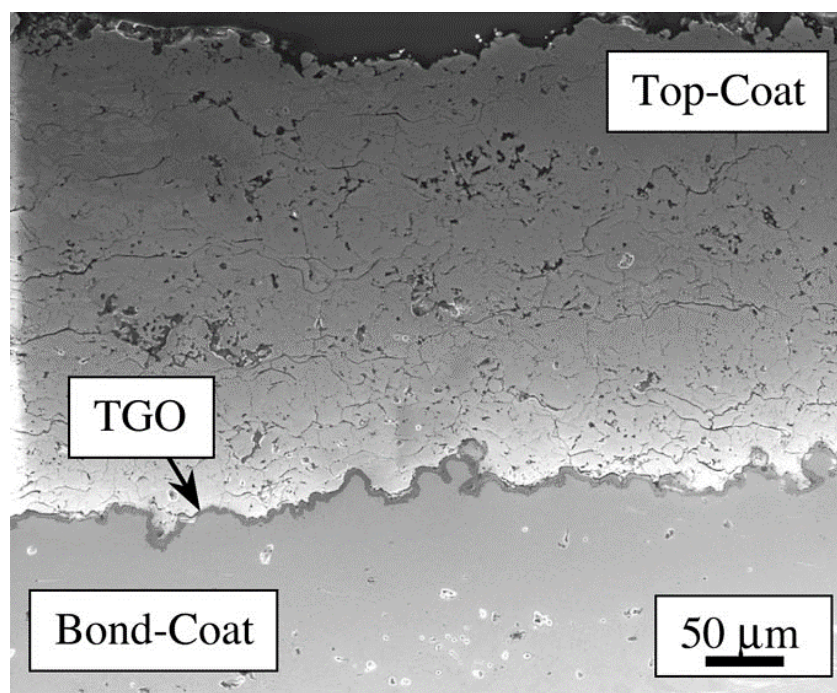

Figure 13. Cross-sectional SEM of an air-plasma sprayed (APS) TBC that has been subjected to 120 thermal cycles (reproduced with permission from [58], The American Association for the Advancement of Science, 2002).

2.3. Durability According to Structure of Thermal Barrier Coatings

The microstructures of TBCs contain pores and are largely classified into lamellar structures and vertical structures. These microstructures are known to form various coating structures depending on the size of the powder and the spraying conditions (spray distance, current value, spray rate, etc.) in the coating method [69]. In addition, as the structure is changed, the thermal structure and thermal stress in the coating in the operating environment are altered, which changes the durability performance accordingly. Structural factors affecting durability include thickness, cracks in coatings, pores, and TGO shapes, and studies on the effect of each factor have been conducted. An understanding of the durability performance according to the detailed structural shape of the TBC is necessary for the development of efficient coatings.

The thickness of the top coating and the bond coating can be adjusted when manufacturing the TBC. In general, as the thickness of the TBC increases, the thermal barrier performance improves and the thermal stress generated between the top coating and the bond coating interface is reduced. Figure 14 shows the results of variations in the top coating-TGO interfacial stress (S11) as the thickness of the top coating changes from 200–800 μm. However, excessively thick coatings cannot be applied to turbines such as combustors, high pressure turbine (HPT) blades, and HPT nozzles in commercial and military jet engines because of the strong centrifugal forces generated at high speeds of rotations above 3000 RPM. Even if the coating is applied, the durability of the coating is reduced because the residual stress formed by the TBC manufacturing process increases [70–73].
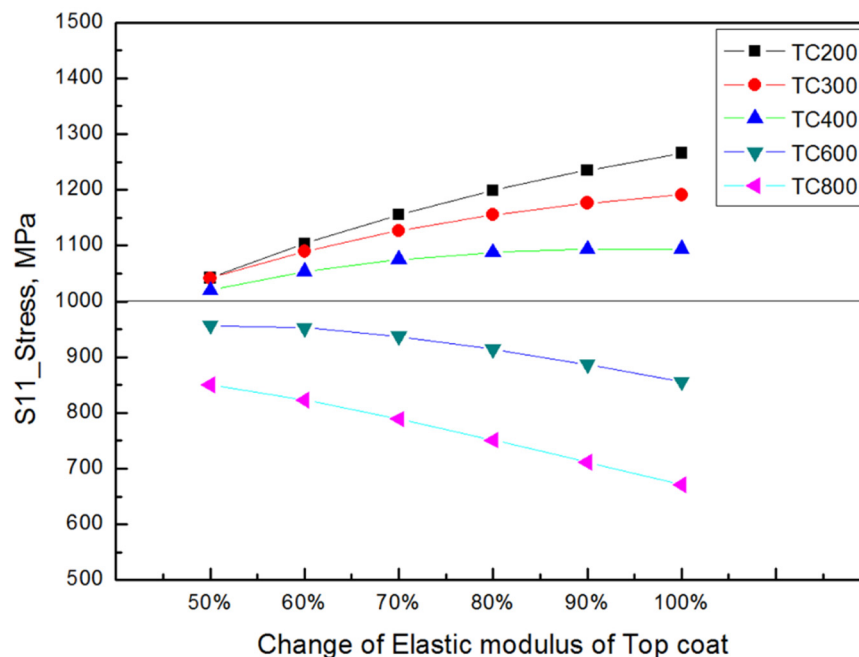

Figure 14. Stress variation according to the thickness of TBC.

Cracks present in the top coating may cause the TBC to fail, but vertical cracks artificially inserted in the coating manufacturing process increase the durability of the TBC. DVC and solution precursor plasma spray (SPPS) coatings that form a dense coating layer using small particles and then thermally impact the coating layer using a relatively low temperature plasma have internal vertical cracks. These vertical cracks improve the durability and life of the coating by reducing thermal stresses caused by repeated thermal fatigue expansion and contraction.

Figure 15 shows the results of FE analysis, performed by Wang et al. [74], of the stress intensity factor and energy release rate depending on the horizontal and vertical positions and crack lengths of the vertical cracks in the top coating. The stress intensity factor (K_I) and energy release rate (G) increased as the vertical crack position shifted from peak to valley to peak (Figure 15a). Also, as the vertical crack approached TGO (y increased), the stress intensity factor and energy release rate decreased because the TGO layer reduces stress concentration (Figure 15b). In addition, as the crack length increases, stress intensity factor and energy release rate increase (Figure 15c), which is consistent with the theory of linear elastic fracture mechanics [74].
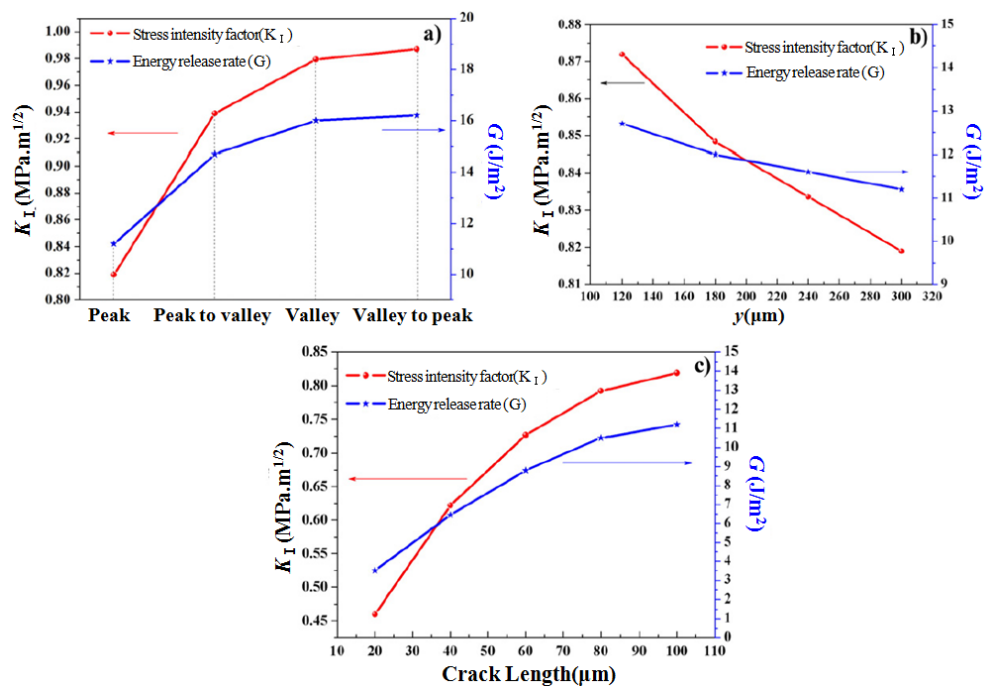
Figure 15. The stress intensity factor and energy release rate of the vertical crack as the function of the position in the (**a**) x-direction, (**b**) y-direction, and (**c**) the length of the vertical crack (reproduced with permission from [74], Elsevier, 2016).

Among the TBC structures, pores exist mainly in the top coating, which is a ceramic material. Increasing the amount of pores decreases the thermal conductivity of the top coating, thereby reducing the heat transfer to the base material and reducing the thermal stress at the bond and top coating interfaces, thus increasing the thermal fatigue life of the TBC. However, if excessive pores are present, reducing the adhesion between the top coating and the bond coating becomes problematic. Therefore, the pores present in the coating layer should be adjusted according to the use environment of the component to which the TBC is applied. In general, in the case of a coating layer manufactured by the spray coating method, many pores exist, and a large powder size and hollow powder are used to obtain a porous coating layer in which more pores are present. In addition, the shape and distribution of the pores affects the performance and properties of the TBC [75]. Figure 16 shows the analysis results of Young's modulus, which depend on porosity, obtained in a study by Jang et al. [76]. The surface regions of the coating maintain a constant value regardless of the pores, but in the side regions, the Young's modulus decreases as the pores increase, which means that the Young's modulus of the coating is highly dependent on the porosity and microstructure [76].
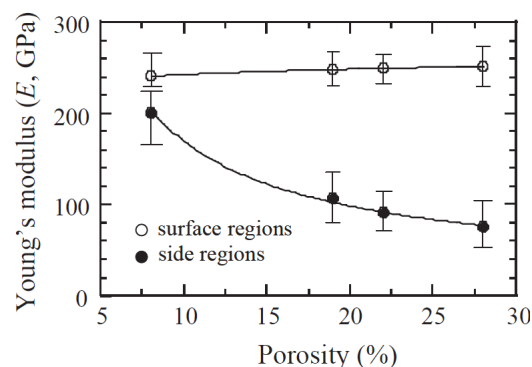

Figure 16. Young's modulus as function of porosity for ZrO_2-4 mol% Y_2O_3 coatings (reproduced with permission from [76], Elsevier, 2005).

2.4. Thermal Properties of Thermal Barrier Coatings

2.4.1. Thermal Conductivity of TBC

Because TBCs and superalloys are made of different materials, the mechanism of thermal transport is also different. The lattice vibration, e.g., phonons, is the dominant source of thermal transport in TBC, whereas free electrons, e.g., electrons, contributes to the majority of thermal transport in superalloys. This is caused by the difference between nickel, the main component of the superalloys, which is a metal where thermal transport is dominated by electrons, and zirconia, the main component of the TBC, which is a non-metal. In particular, phonons are scattered owing to the cracks and pores of the TBC, and the mean free path is shortened, thereby lowering the thermal conductivity.

2.4.2. Thermal Conductivity by Material

Materials that can be used in TBCs must satisfy several necessary conditions. The first requirement is low thermal conductivity, the second is mechanical stability with temperature, and the third is the effect of pores inside the material [77]. Polycrystalline oxides used as TBCs have a thermal conductivity of 1–30 W/m-K, depending on the temperature [77,78]. Among them, zirconia (ZrO_2), which shows small thermal conductivity change with temperature and has a thermal conductivity of approximately 2 W/m-K, is mostly used [79].

- Yttria stabilized zirconia

The phase stability of pure zirconia is low because of the phase changes during the heating and cooling processes. Thus, YSZ is used by adding yttria (Y_2O_3). In addition, the higher the amount of yttria used, the lower the thermal conductivity of TBC; this is because of the phonon scattering due to point defects [80]. As the content of yttria in zirconia increases, the thermal conductivity decreases by more than 50%. Because of the thermal repeatability in practical use, zirconia with 7 wt.% yttria, 7YSZ, is mostly used, which was developed by NASA in the 1970s via burner league tests.

- Zirconia with rare earth

Currently, research on zirconia $M_2Zr_2O_7$ (M is a rare earth element) including rare earths is being actively conducted [81]. Rare earths are used because they increase the durability of TBCs, increase the acceptable temperature of turbine entry temperature, and use smaller thicknesses than conventional TBCs. The thermal conductivity of TBC using rare earths is low owing to the short phonon mean free path.

EB-PVD TBCs with a thickness of 250 μm, including 4 mol% rare earth metals, such as Gadolinia, Neodymia, and Ytterbia, have thermal conductivities of approximately 1 W/m-K at room temperature, and those of 0.88, 1.00, and 1.02 W/m-K at 500 °C, respectively [79].

2.4.3. Thermal Conductivity Dependence on Various Deposition Method

In the APS method, the powder has a layered structure in which layers are stacked in the form of flat agglomerates on the superalloys, and contains several pores, which causes the thermal conductivity of the TBC to be 0.8–1.1 W/m-K depending on the temperature mainly owing to the pores in the structure. LPPS is a method of depositing high temperature plasma, similar to APS, at a low pressure in the chamber during deposition. The reason for maintaining a low-pressure environment is to increase the mechanical strength of the TBC by minimizing the air layer mixed with the pores. The thermal conductivity of TBCs deposited by the LPPS method is 2–6 W/m-K, depending on the temperature. This thermal conductivity is higher than that achieved by the APS method because the air layer inside the TBC is minimized through the deposition at low pressure, thereby reducing the porosity and density. Compared to the APS method, the LPPS method has an advantage as it achieves a higher mechanical strength. However, the process is difficult and results in a slightly higher thermal conductivity than that of the APS method, which is a disadvantage when considering the thermal barrier. In the plasma spray

method, the parameters that can be controlled during deposition vary with plasma gas, plasma power, nozzle diameter, the grain size, the distance between the spray and the base material, the temperature of the base material, and the roughness of the superalloy. The grain size is directly related to thermal conductivity. The changes in thermal conductivity according to the grain size have been studied using simulations [79,80]. As the grain size of the TBC decreases and becomes smaller than the mean free path of the phonon, the thermal conductivity decreases because scattering occurs.

The EB-PVD method vaporizes the deposition material using an electron beam in a vacuum chamber. TBCs formed using the EB-PVD method are deposited on superalloys with a columnar structure. The thermal conductivity of TBCs deposited using this method is 1.5–1.9 W/m-K, depending on the temperature. If only thermal conductivity is considered, the APS method with a layered structure achieves a lower thermal conductivity than EB-PVD method with a columnar structure, thereby improving the thermal barrier performance. However, because the EB-PVD method achieves a very good mechanical strength due to the internal structure of the TBC, many studies have been conducted on methods to lower the thermal conductivity using EB-PVD.

2.4.4. Thermal Conductivity Dependence on Deposition Shape

Several methods have been proposed to fabricate TBCs with low thermal conductivity while using EB-PVD to achieve high corrosion resistance and durability. The method of repeatedly depositing each column of the columnar structure with two materials has been presented (Figure 17a). Thermal conductivity can be reduced by 25% using this method. In the EB-PVD deposition method, the superalloy is tilted at a certain angle and rotated to form a zig-zag columnar structure to induce the scattering of phonons (Figure 17b). This approach reduces the thermal conductivity by up to 40% [82], which increases the blade's acceptable temperature. The thermal conductivity of the TBC can be lowered by inserting impurities into zirconia to induce scattering of phonons due to point defects or by repeatedly depositing different materials.
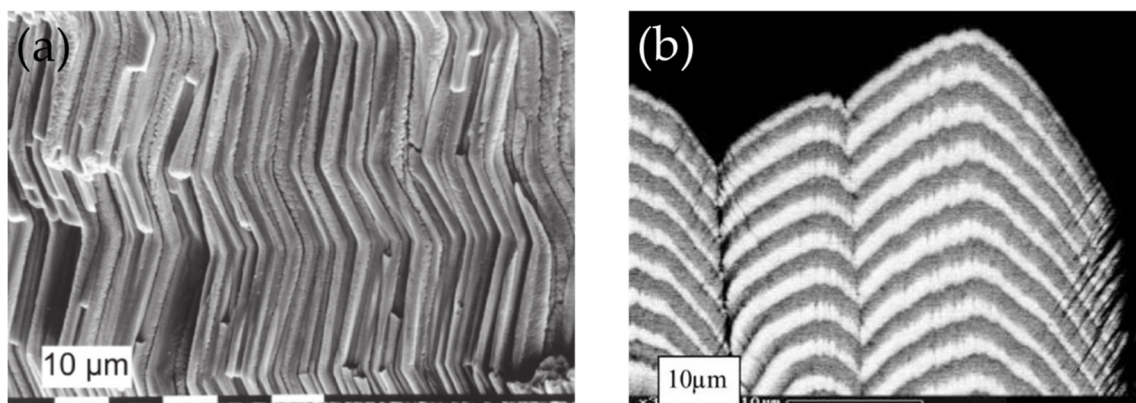

Figure 17. (**a**) Zig-zag structured (reproduced with permission from [82], John Wiley and Sons, 2005) and (**b**) multilayered EB-PVD TBC (reproduced with permission from [83], Elsevier, 2000).

3. Summary

In this paper, a comprehensive review on superalloys and thermal barrier coating (TBC) used as gas turbine blade materials was performed. The manufacturing processes of superalloys have been developed in order of wrought process, conventional investment casting, directional solidification, and single crystal casting to cope with the improvement of the gas turbine inlet temperature. In case of single crystal alloys, Re and Ru were added to improve high temperature properties, and the generations are classified according to their amount of addition. However, considering the high cost of Re and Ru, recently, alloys having excellent high temperature properties with low Re and Ru are being developed. The composition and mechanical properties, especially tensile and creep properties

of typical alloys in each casting process and generation were described. In order to improve creep property by reducing grain boundaries perpendicular to the stress axis, directional solidification in the [001] direction is induced by the Bridgman method. Only one grain remains while passing through the selector during directional solidification, which leads to single crystal. In addition, the applicability of various models to the life prediction of creep, which is a major cause of failure of blades, was examined. The TBC has a different microstructure depending on the manufacturing process (EB-PVD, CVD, APS), and the properties of each process and microstructure through SEM images were analyzed. The thermal barrier coating has a close relationship with durability and mechanical and thermal properties depending on the structure. As the thickness of the coating increases, the heat resistance performance increases, but due to the strong centrifugal force, there are limitations on the thickness that can be applied. The vertical crack inserted in the top coating reduces the stress caused by thermal expansion to improve the durability of the coating. The pores present in the coating play a role in reducing the thermal conductivity, but excessive amounts of pores may instead act as a cause of deteriorating mechanical properties. Phonons are the dominant factor in heat transfer of thermal barrier coating. Phonon scattering occurs due to cracks and pores, and the mean free path is shortened to lower thermal conductivity. If only the thermal conductivity is considered, the thermal barrier performance generated by the APS process is evaluated higher than that of the EB-PVD process. Since the thermal barrier coating has different structures and different mechanical and thermal properties, it is essential to select the appropriate process and to understand the coating structure when applying the thermal barrier coating or designing and developing a new thermal barrier coating. Overall, this review should serve as a reference for further enhancing the TET of the gas turbine for power plants or aviation in the future.

Conflicts of Interest: The authors declare no conflict of interest.

References

1. King, D.; Inderwildi, O.; Carey, C. Advanced aerospace materials: Past, present and future. *Aviat. Space Environ.* **2009**, *3*, 22–27.
2. Yoo, Y.S. Nickel base superalloys. *Korean J. Chem. Eng.* **2014**, *17*, 1–9.
3. Wahl, J.B.; Harris, K. New single crystal superalloys, CMSX®-8 and CMSX®-7. In Proceedings of the ASME Turbo Expo 2014: Turbine Technical Conference and Exposition, Düsseldorf, Germany, 16–20 June 2014.
4. INCO. *Alloy IN-738 Technical Data*; The International Nickel Company, Inc.: New York, NY, USA. Available online: https://www.nickelinstitute.org/media/1709/in_738alloy_preliminarydata_497_.pdf (accessed on 7 August 2020).
5. Kaufman, M. Properties of cast Mar-M-247 for Turbine Blisk applications. *Superalloys* **1984**, 43–52. [CrossRef]
6. Kattus, J.R. *Aerospace Structural Metals Handbook*; Purdue Research Foundation: West Lafayette, IN, USA, 1999; Code 4218; p. 4.
7. Fritz, L.J.; Koster, W.P. *Tensile and Creep Rupture Properties of (1) Uncoated and (2) Coated Engineering Alloys at Elevated Temperatures*; NASA Technical Report, NAS CR-135138; NASA: Washington, DC, USA, 1977.
8. Harris, K.; Erickson, G.L.; Schwer, R.E.; Committee, A.H. Directionally solidified and single-crystal superalloys. In *Properties and Selection: Irons, Steels, and High-Performance Alloys*; ASM International: Cleveland, OH, USA, 1990; Volume 1, pp. 995–1006.
9. Harris, K.; Erickson, G.L.; Schwer, R.E. MAR M 247 derivations—CM 247 LC DS alloy, CMSX®single crystal alloys, properties and performance. *Superalloys* **1984**, 43–52. [CrossRef]

10. Caruel, F.; Bourguignon, S.; Lallement, B.; Fargeas, S.; DeBussac, A.; Harris, K.; Erickson, G.L.; Wahl, J.B. SNECMA experience with cost-effective DS airfoil technology applied using CM 186 LC®Alloy. *J. Eng. Gas. Turbines Power* **1998**, *120*, 97–104. [CrossRef]

11. Erickson, G.L.; Harris, K.; Schwer, R.E. Directionally solidified DS CM 247 LC—optimized mechanical properties resulting from extensive γ′ solutioning. In Proceedings of the ASME 1985 International Gas Turbine Conference and Exhibit, Houston, TX, USA, 18–21 March 1985.

12. Khan, T.; Caron, P.; Fournier, D.; Harris, K. Single crystal superalloy for turbine blades: Characterization and optimization of CMSX-2 alloy. *Mater. Technol.* **1985**, 567–578. [CrossRef]

13. Ross, E.W.; O'Hara, K.S. Rene N4: A first generation single crystal turbine airfoil alloy with improved oxidation resistance, low angle boundary strength and superior long time rupture strength. *Superalloys* **1996**, 19–25. [CrossRef]

14. Cetel, A.; Duhl, D. Second-generation nickel-base single crystal superalloy. *Superalloys* **1988**, 235–244. [CrossRef]

15. Cetel, A.; Duhl, D. Second generation columnar grain nickel-base superalloy. *Superalloys* **1992**, 287–296. [CrossRef]

16. Tsao, T.K.; Yeh, A.C.; Kuo, C.M.; Kakehi, K.; Murakami, H.; Yeh, J.W.; Jian, S.R. The high temperature tensile and creep behaviors of high entropy superalloy. *Sci. Rep.* **2017**, *7*, 12658. [CrossRef]

17. Miner, R.V.; Gabb, T.P.; Gayda, J.; Hemker, K.J. Orientation and temperature dependence of some mechanical properties of the single-crystal nickel-base superalloy René N4: Part III. Tension-compression anisotropy. *Met. Mater. Trans. A* **1986**, *17*, 507–512. [CrossRef]

18. Duhl, D.N.; Cetel, A.D. Superalloy Single Crystal Articles. U.S. Patent 4 402 772, 6 September 1983.

19. Corrigan, J.; Launsbach, M.G.; Mihalisin, J.R. Nickel Base Superalloy and Single Crystal Castings. U.S. Patent 8 241 560, 14 August 2012.

20. Erickson, G. The development and application of CMSX-10. *Superalloys* **1996**, 35–44. [CrossRef]

21. Walston, W.; O'Hara, K.; Ross, E.; Pollock, T.; Murphy, W. Rene' N6: Third generation single crystal superalloy. *Superalloys* **1996**, 27–34. [CrossRef]

22. Kobayashi, T.; Koizumi, Y.; Nakazawa, S.; Yamagata, T.; Harada, H. Design of high rhenium containing single crystal superalloys with balanced intermediate and high temperature creep strengths. In *Advances in Turbine Materials, Design and Manufacturing*; Strang, A., Ed.; The Institute of Materials: London, UK, 1997; p. 766.

23. Yeh, A.C.; Tin, S. Effects of Ru on the high-temperature phase stability of Ni-base single crystal superalloys. *Metall. Mater. Trans. A* **2006**, *37*, 2621–2631. [CrossRef]

24. O'Hara, K.S.; Walston, W.S.; Ross, E.W.; Darolia, R. GE Company. U.S. Patent 5 482 789, 9 January 1996.

25. Yokokawa, T.; Osawa, M.; Nishida, K.; Kobayashi, T.; Koizumi, Y.; Harada, H. Partitioning behavior of platinum group metals on the γ and γ′ phases of Ni-base superalloys at high temperatures. *Scr. Mater.* **2003**, *49*, 1041–1046. [CrossRef]

26. *Fourth Generation Nickel Base Single Crystal Superalloy TMS-138/138A*; National Institute for Materials Science: Tsukuba, Japan, 2006.

27. Caron, P. High γ′ solvus new generation nickel-based superalloys for single crystal turbine blade applications. *Superalloys* **2000**, 737–746. [CrossRef]

28. Sato, A.; Harada, H.; Yeh, A.C.; Kawagishi, K.; Kobayashi, T.; Koizumi, Y.; Yokokawa, T.; Zhang, J.X. A 5th generation SC superalloy with balanced high temperature properties and processability. *Superalloys* **2008**, 131–138. [CrossRef]

29. Koizumi, Y.; Osawa, M.; Kobayashi, T.; Yokokawa, T.; Zhang, J.; Harada, H.; Aoki, Y.; Arai, M. Development of next-generation Ni-base single crystal superalloys. *Superalloys* **2004**, 35–43.

30. Kawagishi, K.; Yokokawa, T.; Kobayashi, T.; Koizumi, Y.; Sakamoto, M.; Yuyama, M.; Harada, H.; Okada, I.; Taneike, M.; Oguma, H. Development of low or zero-rhenium high-performance Ni-base single crystal superalloys for jet engine and power generation applications. *Superalloys* **2016**, 115–122. [CrossRef]

31. Available online: https://www.questek.com/wp-content/uploads/2020/05/SXOverview.pdf (accessed on 5 August 2020).

32. Rettig, R.; Matuszewski, K.; Müller, A.; Helmer, H.E.; Ritter, N.C.; Singer, R.F. Development of a Low-Density Rhenium-Free Single Crystal Nickel-Based Superalloy by Application of Numerical Multi-Criteria Optimization Using Thermodynamic Calculations. *Superalloys* **2016**, 35–44. [CrossRef]

33. Seo, S.M.; Kim, I.S.; Lee, J.H.; Jo, C.Y.; Miyahara, H.; Ogi, K. Grain structure and texture evolutions during single crystal casting of the Ni-base superalloy CMSX-4. *Met. Mater. Int.* **2009**, *15*, 391–398. [CrossRef]

34. Pollock, T.M.; Tin, S. Nickel-based superalloys for advanced turbine engines: Chemistry, microstructure and properties. *J. Propuls. Power* **2006**, *22*, 361–374. [CrossRef]

35. Chen, S.H.; Su, S.C.; Chang, P.C.; Chou, S.Y.; Shieh, K.K. The machinability of MAR-M247 superalloy. *Adv. Eng. Forum* **2011**, *1*, 155–159. [CrossRef]

36. Polvorosa, R.; Suárez, A.; De Lacalle, L.N.L.; Cerrillo, I.; Wretland, A.; Veiga, F. Tool wear on nickel alloys with different coolant pressures: Comparison of Alloy 718 and Waspaloy. *J. Manuf. Process.* **2017**, *26*, 44–56. [CrossRef]

37. Suárez, A.; Veiga, F.; De Lacalle, L.N.L.; Polvorosa, R.; Lutze, S.; Wretland, A. Effects of ultrasonics-assisted face milling on surface integrity and fatigue life of Ni-Alloy 718. *J. Mater. Eng. Perform.* **2016**, *25*, 5076–5086. [CrossRef]

38. Suárez, A.; De Lacalle, L.N.L.; Polvorosa, R.; Veiga, F.; Wretland, A. Effects of high-pressure cooling on the wear patterns on turning inserts used on Alloy IN718. *Mater. Manuf. Process.* **2016**, *32*, 678–686. [CrossRef]

39. Suárez, A.; Veiga, F.; Polvorosa, R.; Artaza, T.; Holmberg, J.; De Lacalle, L.N.L.; Wretland, A. Surface integrity and fatigue of non-conventional machined Alloy 718. *J. Manuf. Process.* **2019**, *48*, 44–50. [CrossRef]

40. Avala, L.; Bheema, M.; Singh, P.K.; Rai, R.K.; Srivastava, S. Mearurement of thermos physics properties of nickel based superalloys. *IJMER* **2013**, *1*, 108–121. [CrossRef]

41. Zieliñska, M.; Yavorska, M.; Porêba, M.; Sieniawski, J. Thermal properties of cast nickel based superalloys. *Arch. Mater. Sci. Eng.* **2010**, *44*, 35–38.

42. Terada, Y.; Ohkubo, K.; Miura, S.; Sanchez, J.M.; Mohri, T. Thermal conductivity and thermal expansion of Ir3X (X = Ti, Zr, Hf, V, Nb, Ta) compounds for high-temperature applications. *Mater. Chem. Phys.* **2003**, *80*, 385–390. [CrossRef]

43. Przeliorz, R.; Piątkowski, J. Application of DSC method in studies on phase transitions of Ni Superalloys. *Arch. Foundry Eng.* **2017**, *17*, 133–136. [CrossRef]

44. Quested, P.N.; Brooks, R.F.; Chapman, L.; Morrell, R.; Youssef, Y.; Mills, K.C. Measurement and estimation of thermophysical properties of nickel based superalloys. *Mater. Sci. Technol.* **2009**, *25*, 154–162. [CrossRef]

45. Wang, Q.; Yang, M.; Song, X.L.; Jia, J.; Xiang, Z. Rationalization of creep data of creep-resistant steels on the basis of the new power law creep equation. *Met. Mater. Trans. A* **2016**, *47*, 3479–3487. [CrossRef]

46. Kim, W.G.; Yin, S.N.; Kim, S.H.; Ryu, W.S.; Lee, C.B.; Kim, S.J. A numerical approach to determine creep constants for Time-Temperature Parametric methods. *Met. Mater. Int.* **2009**, *15*, 559–564. [CrossRef]

47. Kim, S.C.; Shim, J.H.; Jung, W.-S.; Choi, Y.S. Short-term creep data based long-term creep life predictability for grade 92 steels and its microstructural basis. *Met. Mater. Int.* **2018**, *25*, 713–722. [CrossRef]

48. Abdallah, Z.; Perkins, K.; Arnold, C. Creep lifing models and techniques. *Creep* **2018**, *115*. [CrossRef]

49. Abdallah, Z.; Gray, V.; Whittaker, M.; Perkins, K. A Critical analysis of the conventionally employed creep lifing methods. *Materials* **2014**, *7*, 3371–3398. [CrossRef]

50. Whittaker, M.T.; Harrison, W. Evolution of Wilshire equations for creep life prediction. *Mater. High. Temp.* **2014**, *31*, 233–238. [CrossRef]

51. Yang, M.; Wang, Q.; Song, X.L.; Jia, J.; Xiang, Z. On the prediction of long term creep strength of creep resistant steels. *Int. J. Mater. Res.* **2016**, *107*, 133–138. [CrossRef]

52. Wilshire, B.; Scharning, P.; Hurst, R. A new approach to creep data assessment. *Mater. Sci. Eng. A* **2009**, *510*, 3–6. [CrossRef]

53. Wilshire, B.; Scharning, P. Long-term creep life prediction for a high chromium steel. *Scr. Mater.* **2007**, *56*, 701–704. [CrossRef]

54. Gleeson, B. Thermal barrier coatings for aeroengine applications. *J. Propuls. Power* **2006**, *22*, 375–383. [CrossRef]

55. Liu, Q.; Huang, S.; He, A. Composite ceramics thermal barrier coatings of yttria stabilized zirconia for aero-engines. *J. Mater. Sci. Technol.* **2019**, *35*, 2814–2823. [CrossRef]

56. Lepeshkin, A. Investigations of thermal barrier coatings for turbine parts. In *Ceramic Coatings–Applications in Engineering*; IntechOpen: London, UK, 2012.

57. Evans, A.; Mumm, D.; Hutchinson, J.; Meier, G.; Pettit, F. Mechanisms controlling the durability of thermal barrier coatings. *Prog. Mater. Sci.* **2001**, *46*, 505–553. [CrossRef]

58. Padture, N.P. Thermal barrier coatings for gas-turbine engine applications. *Science* **2002**, *296*, 280–284. [CrossRef]

59. Fernández-Abia, A.; Barreiro, J.; Fernández-Larrinoa, J.; Fernández-Valdivielso, A.; Pereira, O.; De Lacalle, L.N.L. Behaviour of PVD coatings in the turning of austenitic stainless steels? *Procedia Eng.* **2013**, *63*, 133–141. [CrossRef]

60. Schulz, U.; Nowotnik, A.; Kunkel, S.; Reiter, G. Effect of processing and interface on the durability of single and bilayer 7YSZ / gadolinium zirconate EB-PVD thermal barrier coatings. *Surf. Coatings Technol.* **2020**, *381*, 125107. [CrossRef]

61. Zhang, B.; Chen, K.; Baddour, N.; Patnaik, P. Failure and life evaluation of EB-PVD thermal barrier coatings using temperature-process-dependent model parameters. *Corros. Sci.* **2019**, *156*, 1–9. [CrossRef]

62. Jing, F.; Yang, J.; Yang, Z.; Zeng, W. Critical compressive strain and interfacial damage evolution of EB-PVD thermal barrier coating. *Mater. Sci. Eng. A* **2020**, *776*, 139038. [CrossRef]

63. Craig, M.; Ndamka, N.; Wellman, R.; Nicholls, J. CMAS degradation of EB-PVD TBCs: The effect of basicity. *Surf. Coat. Technol.* **2015**, *270*, 145–153. [CrossRef]

64. Vargas-García, J.; Goto, T. Thermal barrier coatings produced by chemical vapor deposition. *Sci. Technol. Adv. Mater.* **2003**, *4*, 397–402. [CrossRef]

65. Chen, L.; Goto, T.; Hirai, T. Preparation of silicon carbide powders by chemical vapor deposition. *Yogyo Kyokai-Shi* **1988**, *91*, 49–54. [CrossRef]

66. Goto, T. Thermal barrier coatings deposited by laser CVD. *Surf. Coat. Technol.* **2005**, *198*, 367–371. [CrossRef]

67. De Lacalle, L.L.; Gutierrez, A.; Lamikiz, A.; Fernandes, M.H.; Sanchez, J.A.; Lamikiz, A. Turning of thick thermal spray coatings. *J. Therm. Spray Technol.* **2001**, *10*, 249–254. [CrossRef]

68. Rajendran, R. Gas turbine coatings–An overview. *Eng. Fail. Anal.* **2012**, *26*, 355–369. [CrossRef]

69. Kwak, C.W. Thermal barrier coating technology and application. *Ceramist* **2016**, *19*, 46–56.

70. Abedi, H.; Salehi, M.; Shafyei, A. Microstructural, mechanical and thermal shock properties of triple-layer TBCs with different thicknesses of bond coat and ceramic top coat deposited onto polyimide matrix composite. *Ceram. Int.* **2018**, *44*, 6212–6222. [CrossRef]

71. Ziaei-Asl, A.; Ramezanlou, M.T. Thermo-mechanical behavior of gas turbine blade equipped with cooling ducts and protective coating with different thicknesses. *Int. J. Mech. Sci.* **2019**, *150*, 656–664. [CrossRef]

72. Ramezanlou, M.T. Effects of thermal barrier coating (TBC) thickness on temperature distribution of gas turbine blade. In Proceedings of the 3rd Conference on Advances in Mechanical Engineering Istanbul (ICAME 2017), Istanbul, Turkey, 19–21 December 2017.

73. Yuri, M.; Masada, J.; Tsukagoshi, K.; Ito, E.; Hada, S. Development of 1600 C-class high-efficiency gas turbine for power generation applying J-Type technology. *Mitsubishi Heavy Ind. Tech. Rev.* **2013**, *50*, 1–10.

74. Wang, L.; Yang, J.; Ni, J.; Liu, C.; Zhong, X.; Shao, F.; Zhao, H.; Tao, S.; Wang, Y. Influence of cracks in APS-TBCs on stress around TGO during thermal cycling: A numerical simulation study. *Surf. Coat. Technol.* **2016**, *285*, 98–112. [CrossRef]

75. Schlichting, K.W.; Padture, N.P.; Klemens, P.G. Thermal conductivity of dense and porous yttria-stabilized zirconia. *J. Mater. Sci.* **2001**, *36*, 3003–3010. [CrossRef]

76. Jang, B.K.; Matsubara, H. Influence of porosity on hardness and Young's modulus of nanoporous EB-PVD TBCs by nanoindentation. *Mater. Lett.* **2005**, *59*, 3462–3466. [CrossRef]

77. Clarke, D. Materials selection guidelines for low thermal conductivity thermal barrier coatings. *Surf. Coat. Technol.* **2003**, *163*, 67–74. [CrossRef]

78. Kingery, W.D. Thermal conductivity: XII, temperature dependence of conductivity for single-phase ceramics. *J. Am. Ceram. Soc.* **1955**, *38*, 251–255. [CrossRef]

79. Nicholls, J.; Lawson, K.; Johnstone, A.; Rickerby, D. Methods to reduce the thermal conductivity of EB-PVD TBCs. *Surf. Coat. Technol.* **2002**, *151*, 383–391. [CrossRef]

80. Klemens, P.; Gell, M. Thermal conductivity of thermal barrier coatings. *Mater. Sci. Eng. A* **1998**, *245*, 143–149. [CrossRef]

81. Wu, J.; Wei, X.; Padture, N.P.; Klemens, P.G.; Gell, M.; Garcia, E.; Miranzo, P.; Osendi, M.I. Low-thermal-conductivity rare-earth zirconates for potential thermal-barrier-coating applications. *J. Am. Ceram. Soc.* **2002**, *85*, 3031–3035. [CrossRef]

82. Schulz, U.; Saruhan, B.; Fritscher, K.; Leyens, C. Review on advanced EB-PVD ceramic topcoats for TBC applications. *Int. J. Appl. Ceram. Technol.* **2005**, *1*, 302–315. [CrossRef]
83. Schulz, U.; Fritscher, K.; Leyens, C. Two-source jumping beam evaporation for advanced EB-PVD TBC systems. *Surf. Coat. Technol.* **2000**, *133*, 40–48. [CrossRef]